OXFORD

*Cerebral Cortex*, 2024, **34**, 1–11
https://doi.org/10.1093/cercor/bhae016
Advance access publication date 31 January 2024
**Original Article**

# A radiomics-based brain network in T1 images: construction, attributes, and applications

Han Liu[1,2,†], Zhe Ma[3,2,†], Lijiang Wei[2,4,†], Zhenpeng Chen[2], Yun Peng[1,*,‡], Zhicheng Jiao[5], Harrison Bai[6], Bin Jing[2,*,‡]

[1]Department of Radiology, Beijing Children's Hospital, Capital Medical University, National Center for Children's Health, No. 56, Nanlishilu Road, Xicheng District, Beijing 100045, China,
[2]Beijing Key Laboratory of Fundamental Research on Biomechanics in Clinical Application, School of Biomedical Engineering, Capital Medical University, No. 10, Xitoutiao Youanmenwai, Fengtai District, Beijing 100069, China,
[3]Department of Radiology, Henan Cancer Hospital, The Affiliated Cancer Hospital of Zhengzhou University, 127 Dongming Road, Jinshui District, Zhengzhou, Henan 450008, China,
[4]State Key Laboratory of Cognitive Neuroscience and Learning, Beijing Normal University, No. 19, Xinjiekouwai Street, Haidian District, Beijing 100875, China,
[5]Department of Diagnostic Imaging, Brown University, 593 Eddy Street, Providence, Rhode Island 02903, United States,
[6]Department of Radiology and Radiological Sciences, Johns Hopkins University, 1800 Orleans Street, Baltimore, Maryland 21205, United States

*Corresponding authors: Yun Peng: Department of Radiology, Beijing Children's Hospital, Capital Medical University, National Center for Children's Health, No. 56, Nanlishilu Road, Xicheng District, Beijing 100045, China. Email: ppengyun@yahoo.com; Bin Jing: School of Biomedical Engineering, Capital Medical University, No. 10, Xitoutiao, Youanmenwai, Fengtai District, 100069, Beijing, China. Email: bjing@ccmu.edu.cn

†Han Liu, Zhe Ma, and Lijiang Wei contributed equally.

‡Yun Peng and Bin Jing shared the senior author.

T1 image is a widely collected imaging sequence in various neuroimaging datasets, but it is rarely used to construct an individual-level brain network. In this study, a novel individualized radiomics-based structural similarity network was proposed from T1 images. In detail, it used voxel-based morphometry to obtain the preprocessed gray matter images, and radiomic features were then extracted on each region of interest in Brainnetome atlas, and an individualized radiomics-based structural similarity network was finally built using the correlational values of radiomic features between any pair of regions of interest. After that, the network characteristics of individualized radiomics-based structural similarity network were assessed, including graph theory attributes, test–retest reliability, and individual identification ability (fingerprinting). At last, two representative applications for individualized radiomics-based structural similarity network, namely mild cognitive impairment subtype discrimination and fluid intelligence prediction, were exemplified and compared with some other networks on large open-source datasets. The results revealed that the individualized radiomics-based structural similarity network displays remarkable network characteristics and exhibits advantageous performances in mild cognitive impairment subtype discrimination and fluid intelligence prediction. In summary, the individualized radiomics-based structural similarity network provides a distinctive, reliable, and informative individualized structural brain network, which can be combined with other networks such as resting-state functional connectivity for various phenotypic and clinical applications.

*Key words*: individualized structural similarity network; test–retest reliability; fingerprint; fluid intelligence prediction; mild cognitive impairment discrimination.

## Introduction

The human brain is functioned through the interactions among brain regions, which can be quantified by the noninvasive MRI, making it the most important tool to study the human brain (Jiang 2013). Currently, there are two common MRI modalities to reveal the connective relationships between regions: resting-state functional MRI (rs-fMRI) and diffusion MRI (dMRI), providing crucial insights about the functional and structural connectivity of the whole brain. However, rs-fMRI and dMRI are not routine diagnostic sequences in most clinical scanning, and to collect high-quality data of either sequence is not very easy and needs good cooperation from the subjects, which may further limit their widespread usages in specific populations such as children and neuropsychiatric patients. In contrast, structural MRI (sMRI) is an easy-to-collect sequence that provides high-resolution anatomical information and exhibits a good signal-to-noise ratio and test–retest reliability (Jing et al. 2018; Buimer et al. 2020), making it the most widely collected imaging modality in an open-source neuroimaging dataset.

Usually, the structural network generated from sMRI is the group-level covariance network (Alexander-Bloch et al. 2013; Kuo et al. 2020; Yun et al. 2020) that is constructed with the similarity of morphological features from a group of subjects, but it could not be used for individualized diagnosis and prediction. For this reason, Tijms et al. (2012) firstly proposed an individualized structural network based on the similarity between cubes with $3 \times 3 \times 3$ voxels. After that, several subsequent studies have tried to construct an individualized structural network from different perspectives, and the key ideas behind them could be divided into two categories: (i) directly use some kind of distance metric to quantify the structural similarities between regions, such as Kullback–Leibler similarity (Kong et al. 2014, 2015; Wang et al. 2016), Euclidean distance (Yu et al. 2018; Wang et al. 2020), differential similarity (Liu et al. 2018), and Jensen–Shannon similarity (Li et al. 2021) and (ii) extract multiple morphological features from each region to form a vector and calculate their similarity as the connective value (Li, Yang, et al. 2017; Seidlitz et al. 2018). However, these methods mainly used a few macroscopic

**Received:** November 28, 2023. **Revised:** January 8, 2024. **Accepted:** January 9, 2024

structural descriptors of brain regions, which could not fully reflect individual difference in the brain.

Radiomics is an emerging technology that extracts high-throughput quantitative features from images and has been widely found to correlate with the histological, molecular, and clinical markers in various diseases (Lambin et al. 2017; Liu, Wang, et al. 2019). The radiomic features are multiview, including both macroscopic feature sets (e.g. shape-based feature) and microscopic feature sets (e.g. texture feature). Specifically, the texture features offer voxel-level quantification at different spatial scales within the image, which may reflect the underlying pathophysiological characteristics (Tomaszewski and Gillies 2021). Previously, Zhao, Zheng, et al. (2021) proposed a radiomics-based structural connectivity construction (R2SNs) method and showed impressive attributes and application potentials. Inspired by the idea, we proposed an enhanced individualized radiomics-based structural similarity network (iRSSN) in T1 images. iRSSN takes advantage of the state-of-the-art voxel-based morphometry (VBM) to preprocess the original T1 and uses a selected set of radiomic features to construct the individualized network on gray matter. Specially, comprehensive attributes (e.g. graph theory analysis, test–retest reliability, individual identification, and parameter effect) and applications (e.g. MCI subtype discrimination and fluid intelligence prediction) of iRSSN were evaluated. Taken together, we expect iRSSN can offer a distinctive, reliable, and informative structural network in T1 image, which could be integrated with other types of brain networks to better predict the brain phenotype and brain disease.

# Materials and methods

## Participants

### *Human connectome project dataset*

Data were obtained from Human connectome project (HCP) S1200 release, which included 1,113 high spatial-resolution T1-weighted images and 1,003 high spatial–temporal-resolution rs-fMRI images. Among these subjects, 46 subjects participated in a retest scan. Four subjects in the retest dataset were excluded because one subject did not have fMRI data, one subject did not complete the first session of fMRI scan, and two subjects did not complete the second session of fMRI scan. At last, 42 subjects who completed the entire scan protocol for a second time were used in our study (termed as "Test–Retest dataset"). All images were collected on a 3T Siemens Skyra (Siemens, Erlangen, Germany) scanner. The T1-weighted images and two sessions of the rs-fMRI images were acquired in two consecutive days using MPRAGE sequence and multiband pulse sequence, respectively (TR = 2,400/720 ms, TE = 2.14/33.1 ms, FA = 8/52°, FOV = 224 × 224/208 × 180 $mm^2$, and voxel size = 0.7 × 0.7 × 0.7 $mm^3$/2 × 2 × 2 $mm^3$). The demographic information about the selected 1,003 subjects with both sMRI and rs-fMRI is listed in Table S1 of Supplementary Information.

### *Alzheimer's disease neuroimaging initiative dataset*

A total of 717 mild cognitive impairment (MCI) subjects with T1-weighted structural MRI images were downloaded from the ADNI dataset (https://adni.loni.usc.edu/), including 286 subjects converted to AD (progressive MCI) within 36 months and 431 that did not convert (stable MCI). The detailed demographic information (see Table S2) and inclusion/exclusion criteria are listed in Supplementary information. All data were scanned on 3T MRI systems using MPRAGE sequence (TR = 2,300 ms, TE = 2.95 ms, FA = 9°, TI = 900 ms, slices = 176, and voxel size = 1 × 1 × 1.2 $mm^3$).

### *Multicenter test–retest dataset*

This dataset (Tong et al. 2020) includes three healthy traveling adults that were scanned with identical settings in 10 MRI centers (all 3T MR MAGNETOM Prisma), and the scans were performed by the same operator with a fixed operating procedure. T1-weighted structural images were acquired using an MP2RAGE sequence, and the key parameters were as follows: TR = 5 s, TE = 2.9 ms, FOV = 211 × 256 × 256 $mm^3$, voxel size = 1.2 × 1 × 1 $mm^3$.

## Ethics approval and consent to participate

Ethical approval of ADNI data was obtained by the ADNI investigators. The institutional review boards of all participating sites approved the study at their respective institutions. All ADNI participants provided written informed consent before the start of the study.

All study procedures of the Human Connectome Project study protocol were approved by the Institutional Review Board at the Washington University in St. Louis.

The multicenter test–retest dataset was confirmed by the institutional review board of Xuanwu Hospital, Capital Medical University, Beijing, China, and all volunteers had signed the informed consent forms.

## Definition of iRSSN

Radiomics provides a large number of quantitative imaging features enabling efficient detection of subtle characteristics within images, which may thus be informative for disease diagnosis, prognosis, and treatment responses (Tomaszewski and Gillies 2021). Radiomic features can be divided into macroscopic and microscopic categories, and the macroscopic features describe the holistic characteristics such as shape-related features (e.g. volume, surface area), while microscopic features (e.g. texture) depict the relative relationship with neighbor voxels. In our method, the state-of-the-art VBM (Ashburner 2007; Zhao, Ma, et al. 2021) analysis is adopted to acquire the preprocessed gray matter images, which was conducted by CAT 12 software (Version 12.7, r1700). In detail, the VBM pipeline contains two consecutive parts: initial voxel-based processing and refined voxel-based processing. The first part contains SANLM denoise (Manjon et al. 2010), resampling into anisotropic voxel, initial bias-correction, affine registration, and unified segmentation (Ashburner and Friston 2005), while the second part includes segmentation refinement, skull stripping, regional parcellation, local intensity correction, AMAP/PVE segmentation (Tohka et al. 2004), and Geodesic Shooting registration (Ashburner and Friston 2011). Every subject generated a standardized gray matter image with a 1.5-mm voxel size, which was then smoothed by a 4-mm FWHM Gaussian kernel. After that, the gray matter image was divided into 246 ROIs according to the Brainnetome atlas (Fan et al. 2016), and radiomic features were computed for every ROI of the brain. In previous studies (Wu et al. 2016; Liu, Jing, et al. 2019; Liu et al. 2021), radiomics has been defined with different amounts of feature sets (from dozens to thousands), but many of them may be highly correlated with each other; therefore, only a selected radiomic feature sets were adopted to construct iRSSN. In particular, a total of 43 radiomic features were selected, including 3 first-order features, 9 gray-level co-occurrence matrix (GLCM) features, 13 gray-level run-length matrix (GLRLM) features, 13 gray-level size zone matrix (GLSZM) features, and 5 neighborhood gray-tone difference matrix (NGTDM) features. More detailed description about these features could be found in Vallieres et al. (2015) and Fig. S1 in Supplementary Information. In addition, the calculating

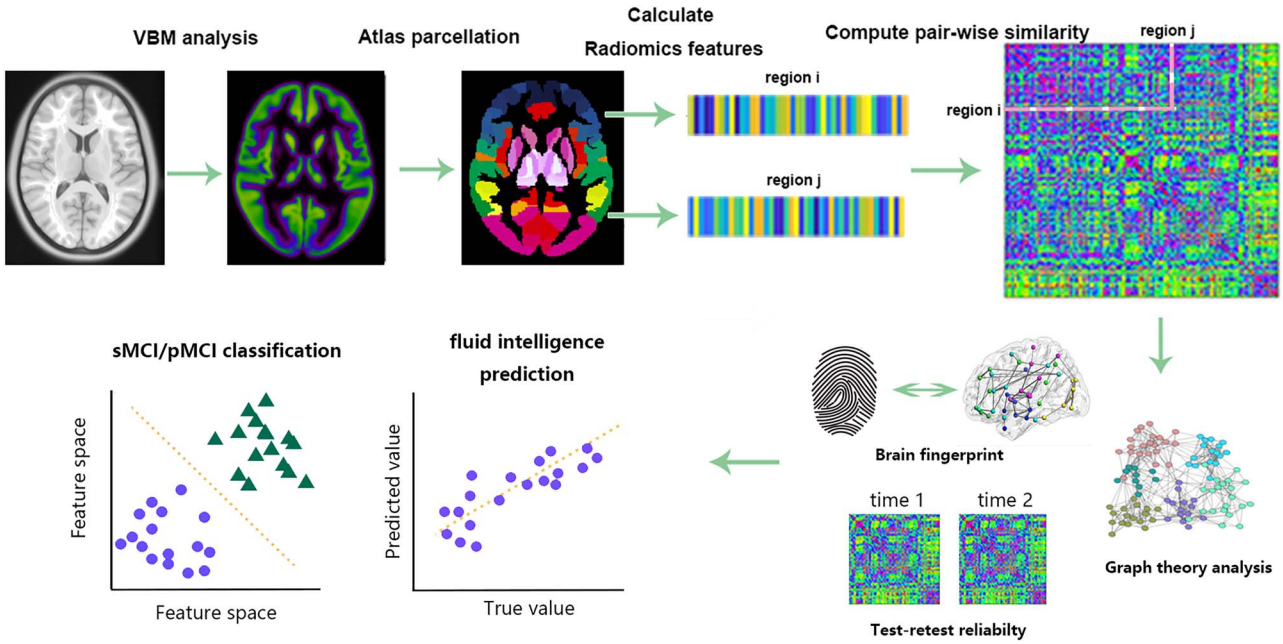


**Fig. 1.** The workflow of the proposed iRSSN.

formula of each radiomic feature were provided in the open-source code (https://github.com/zhema620/iRSSN). After that, the radiomic features of all subject were normalized with a demeaning manner, i.e. for each subject, every radiomic feature of one brain region was divided by its mean value from all brain regions, and the Pearson correlation coefficients were computed between each pairwise ROIs, resulting in an individual 246 × 246 iRSSN matrix for every subject. The whole construction pipeline of iRSSN is illustrated in Fig. 1.

## Characteristics evaluation of iRSSN

### *Graph theory analysis of iRSSN*

To understand the network organization of iRSSN, graph theory analysis was conducted on the HCP dataset to investigate the complex network properties. Four types of network properties were calculated for iRSSN: (i) characteristic path length ($L_p$), clustering coefficient ($C_p$), and small worldness ($\alpha$) (Watts and Strogatz 1998); (ii) global efficiency ($E_g$) and local efficiency ($E_{loc}$) (Latora and Marchiori 2001); (iii) network modularity computed by the greedy algorithm (Newman 2006). The modularity of the network means the nodes within a module are densely connected but sparsely linked to nodes belonging to other modules; and (iv) degree distribution and a network hub that is defined as nodes with more than mean plus two standard deviation (SD) connective edges (Bullmore and Sporns 2009). The detailed definition about these graph metrics are listed in Supplementary information. Given the absence of optimal sparsity threshold, a series of sparsity settings (from 5% to 40% with an interval of 5%) were adopted, and the corresponding complex network attributes were obtained at each sparsity threshold using Brain Connectivity Toolbox (http://www.brain-connectivity-toolbox.net/).

### *Test–retest reliability of iRSSN*

Test–retest reliability quantifies the consistency of one MRI metric on repeated scanning at different time points, and a good MRI biomarker should display high test–retest reliability. The HCP test–retest dataset (42 subjects in 1 center) and multicenter dataset (3 subjects in 10 centers) were adopted to check the test–retest performance of iRSSN, and the intraclass correlation coefficient (ICC) was used to measure the test–retest reliability, which is defined in Supplementary information. Notably, to simplify the visualization of ICC results, ICC values in each region of the Brainnetome atlas were averaged into the Yeo 7 networks and an additional subcortical network (Yeo et al. 2011).

### *Individual identification with iRSSN*

A good MRI biomarker should not only be reliable but also reflect the individual variability. To ascertain the individual identification performance of iRSSN, the HCP test–retest dataset was again used to discover whether iRSSN could distinguish every single subject like fingerprint. The test dataset or retest dataset was alternatively served as a "target" session and the other as a "database" session (Finn et al. 2015). Every subject in the "target" session was used to confirm the most similar subject in the "dataset" session through the Pearson's correlation coefficient of paired iRSSN. If the identified subject matched the target one, its individual identification succeeded; otherwise, it failed. The final accuracy was reported by the average of two identification tasks. To test whether the accuracy was significantly better than random chance, a permutation test ($n = 1{,}000$) was performed on the dataset. Specifically, a random "database" session was created by shuffling individual iRSSN in the database session, and then every subject in the "target" session searched for the most similar subject in the random "database" session. Then, the individual iRSSN of the "database" session was shuffled, and the identification task was similarly performed on the "target" session. The mean accuracy of two identification tasks were averaged as one time of identification result, and the above procedures were repeated 1,000 times to form a null distribution. The $P$-value was defined as the proportion of the accuracy no less than the actual accuracy in the null distribution.

## Potential applications of iRSSN

### *sMCI/pMCI discrimination with iRSSN*

Currently, there are no effective treatment manners for Alzheimer's disease (AD), and it thus becomes a key goal to timely diagnose the high-risk persons due to AD, who will receive benefits from early clinical intervention. Among MCI patients, some will

change into AD in short years, which is called progressive MCI (pMCI), while the others will keep their cognitive abilities in long years, which is named stable MCI (sMCI). Discrimination between pMCI and sMCI patients with MRI is clinically important but challenging (Lian et al. 2020; Zhou et al. 2020). Therefore, this task was selected to exemplify the clinical feasibility of iRSSN in disease classification. The classification pipeline was similar to our previous studies (Ma et al. 2020; Zhao et al. 2021). Basically, the iRSSN-based classification model was constructed with support vector machine (SVM) with "rbf" kernel, and Lasso was used for feature reduction since iRSSN is high dimensional. A grid search method was adopted to ascertain the optimal parameters of SVM ($\gamma$ and C) and Lasso ($\lambda$), and a 10-fold cross-validation was adopted to evaluate the overall performance of the model. It should be mentioned that a stratified sampling based on group label had been used in creating the folds because of the unbalanced sample size in each group, and the optimal parameters were ascertained with an inner 5-fold cross-validation while the testing dataset was completely untouched during the model training. The whole process was repeated 10 times with different training/testing datasets each time, and the final performance was reported by the mean value of sensitivity (Sen), specificity (Spe), accuracy (Acc), and the area under the curve (AUC).

### *Fluid intelligence prediction with iRSSN*

Fluid intelligence represents the ability in reasoning and problem solving, which can be reflected by brain function and structure (Chen et al. 2020; Jiang, Calhoun, et al. 2020; Jiang, Calhoun, et al. 2020; Feng et al. 2022). To validate the application of iRSSN in individual phenotype prediction, 1,003 subjects with both rs-fMRI and structural MRI data were enrolled from the HCP dataset to predict individual fluid intelligence. The whole pipeline was similar to our previous studies (Wei et al. 2020; Feng et al. 2022). First, the covariates including age and gender were regressed out from iRSSN; then, a bootstrapping-based feature selection method (Wei et al. 2020) was used to select the reliable features in training dataset. In the feature selection process, the training dataset was resampled by bootstrap without replacement 100 times and 70% subjects each time. Features that correlated with fluid intelligence ($P < 0.05$, Spearman correlation) at least 90 times in the resampled dataset were finally used to train a Lasso regression model. Specifically, an inner-nested 5-fold cross-validation was used to determine the optimal parameters (i.e. $\lambda$) in the Lasso model. A 10-fold cross-validation on the whole dataset was employed to evaluate the prediction accuracy, and the subjects belonging to the same family was kept in a fold. The prediction performance was assessed by correlating the predicted fluid intelligence with actual values, and the whole procedures were repeated 10 times with different training/testing datasets each time and averaged to gain the final prediction accuracy.

## Comparison with other methods

Resting-state functional connectivity (RSFC) is the most widely used brain network, which is generated from the functional MRI images; therefore, RSFC was selected as the comparison baseline for imaging biomarker attributes. Once iRSSN can be effectively fused with RSFC, i.e. iRSSN provides complementary information to RSFC, it will show great potentials in different disease discrimination/prediction tasks. In the study, we compared iRSSN and RSFC in test–retest reliability, individual identification, and fluid intelligence prediction. Moreover, since some key complex network properties (e.g. small-worldness, modularity, network hub) are qualitative and several previous studies (Achard and Bullmore 2007; Bullmore and Sporns 2009) have already reported them in RSFC, these network properties were not computed for RSFC anymore. For sMCI/pMCI classification, because many subjects in ADNI dataset did not have the resting-state fMRI data, the sMCI/pMCI classification was also not compared between iRSSN and RSFC. The preprocessing steps to generate RSFC can be referred to our previous study (Wei et al. 2020) and were briefly summarized in Supplementary information.

In addition, in order to demonstrate that iRSSN performed better than the conventional morphological metrics in the sMCI/pMCI classification, the atlas-based brain volume information was also used for model construction, and all detailed procedures were consistent with iRSSN except the input features. The brain volume information was obtained by CAT 12 software with Brainnetome atlas, and every subject had a volume vector of 246 regions.

R2SNs (Zhao, Zheng, et al. 2021) is another type of radiomics-based structural network on T1 images, and we compared it thoroughly with iRSSN in both tasks including fluid intelligence prediction and sMCI/pMCI classification. The detailed procedures in prediction/classification model construction were kept the same as iRSSN except the input features, which were generated using the code (https://github.com/YongLiuLab/R2SN_construction).

## Other methodological considerations

A previous study (Wang et al. 2016) had reported that smoothness obviously affected the structural network properties, so the influences of smoothness (smoothed or unsmoothed GM images) on iRSSN were also assessed. Here, we chose the test–retest reliability and sMCI/pMCI classification to exemplify the influence of smoothness. We did not select the fluid intelligence prediction as an evaluation task because our previous study (Feng et al. 2022) had verified a positive relationship between test–retest reliability and the prediction performance.

Next, the effect of feature normalization manner on iRSSN was also evaluated, and three simple feature normalization manners including demeaning, Max-Min, and Max-Min (map into [−1, 1]) were compared in sMCI/pMCI classification. The definitions of the latter two manners are given in Supplementary information. Because all these normalization manners retained the relative magnitude of original features, we did not select the fluid intelligence prediction for evaluation.

# Results

## Graph theory properties of iRSSN

Under different sparsity thresholds (0.05 ~ 0.40) on the HCP dataset, iRSSN displayed approximately equivalent shortest path lengths ($\lambda \approx 1$) and higher clustering coefficients compared with the mean of 1,000 random networks, which implied the prominent small-world properties ($\sigma = \gamma/\lambda > 1$) (Fig. 2A). Moreover, when the sparsity threshold became large, the clustering coefficient ($C_p$), local efficiency ($E_{loc}$), and global efficiency ($E_g$) increased accordingly, while characteristic path length ($L_p$) decreased rapidly (Fig. 2B and C). Here, the clustering coefficient depicts the extent of local cluster or cliquishness of the network, and local/global efficiency measures the extent of information propagation within the local/whole network, while the characteristic path length quantifies the extent of overall routing efficiency of the network (Wang et al. 2009). All these complex network properties of iRSSN displayed comparable patterns with RSFC

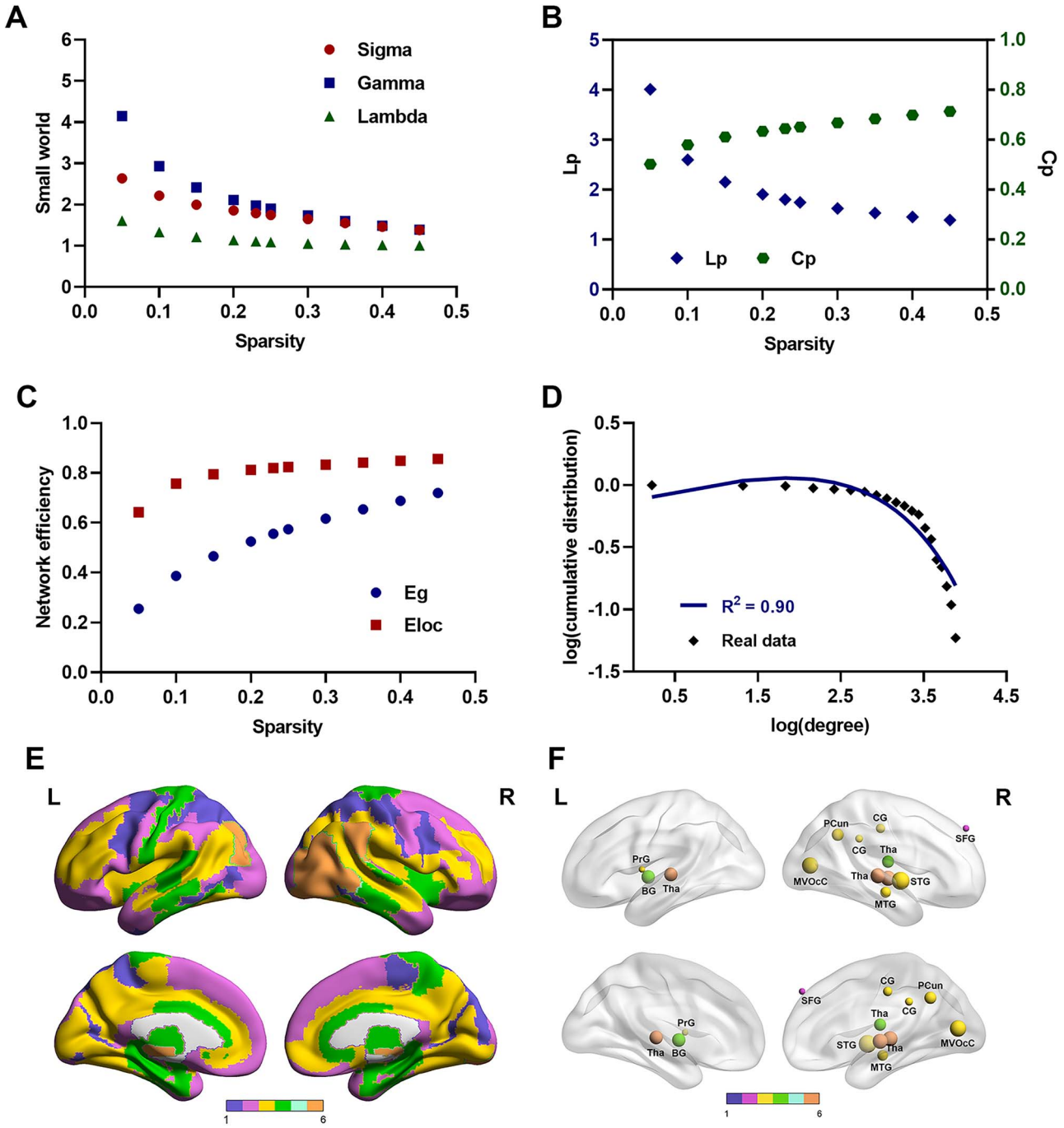


**Fig. 2.** The network properties of iRSSN. A) Small-world properties of the network over a range of sparsity. B) The characteristic path length ($L_p$) and clustering coefficient ($C_p$) of the network. C) Global efficiency ($E_g$) and local efficiency ($E_{loc}$). D) Degree distribution, E) network modularity, and F) the spatial distribution of hubs labelled by the modularity results. Abbreviation: BG, basal ganglia; SFG, superior frontal gyrus; STG, superior temporal gyrus; PrG, precentral gyrus; MTG, middle temporal gyrus; PCun, precuneus; CG, cingulate gyrus; MVOcC, medioventral occipital cortex; Tha, thalamus.

(Achard and Bullmore 2007), indicating that iRSSN may serve as a biologically meaningful structural network.

In addition to complex network properties, the degree distribution of the iRSSN was also fitted using exponential fitting, power law fitting, and exponential truncated power law fitting. The goodness-of-fit (the value closer to 1 indicates a better fitting) for three fitting methods were, respectively, 0.82, 0.47, and 0.90. Thus, the degree distribution was well fitted (Fig. 2D) by an exponentially truncated power-law form: $p^{(k)} = a \times k^{\alpha-1}e^{(-k/k)}$ with an estimated exponent$a = 0.90, \alpha = 1.19, k_c = 34.05$. The distribution indicated that some hub nodes exist in iRSSN, and 13 hub nodes were identified (Fig. 2F), namely the superior frontal gyrus, superior temporal gyrus, precentral gyrus, middle temporal gyrus, precuneus, cingulate gyrus (including two subregions), medioventral occipital cortex, basal ganglia, and thalamus (including four subregions). The detailed position and description about these hub nodes can be found in Supplementary information. Network modularity analysis revealed that the whole brain iRSSN can be divided into six independent modules (Fig. 2E). The spatial distribution of these modules was largely different from the subnetworks of RSFC (Yeo et al. 2011), and the highest spatial overlap was achieved between an iRSSN module and the

dorsal attention network of RSFC with a dice coefficient (defined as 2 × [intersected region]/[sum of region A and region B]) of 0.46. Thus, iRSSN provided a distinct brain network organization complementary to RSFC.

## Test–retest reliability of iRSSN

As shown in Fig. S2, iRSSN showed excellent whole brain reliability (mean ICC = 0.86, SD = 0.08), and more than 90% connective edges showed ICC higher than 0.75. In comparison, the ICC performances of RSFC were lower (mean ICC = 0.58, SD = 0.15), and most connective edges had ICC lower than 0.75. Besides, iRSSN displayed acceptable reliability (mean ICC = 0.60, SD = 0.02) in the multicenter dataset.

## Individual identification with iRSSN

The accuracy of individual identification (brain fingerprint) with iRSSN was 100%, while RSFC had a slightly lower accuracy of 94.05% on the HCP test–retest dataset. In addition, both iRSSN and RSFC displayed significant $P$ values ($P < 0.001$) in the permutation test. The result demonstrated iRSSN displayed fingerprint-like characteristics, which could effectively reveal the individual variability among subjects.

## sMCI/pMCI discrimination with iRSSN

Figure 3A showed the performances of sMCI/pMCI classification by iRSSN, and the accuracy, sensitivity, and specificity were 0.805, 0.729, and 0.855, respectively, with a corresponding AUC of 0.882 (Fig. 3B). A total of 91 connective edges that conserved in every fold of cross-validation (Fig. 3C) were the most discriminative features between sMCI and pMCI patients. Most of the features were internetwork connections, and all eight brain networks were involved in the classification. Moreover, many of the 91 edges were long-range (>75 mm) connections, implying that the network efficiency may be largely reduced in pMCI compared with sMCI. Besides, the subcortical network, ventral attention network, and visual network also displayed some intranetwork alterations in sMCI/pMCI classification, indicating that these networks may be vulnerable to the progressively impaired cognition. Furthermore, several key nodes that connected densely with others (i.e. large radius) in 91 features were also confirmed, mainly including bilateral parahippocampus, right hippocampus, and left superior parietal lobule.

## Fluid intelligence prediction with iRSSN

Figure 3D shows the prediction results for fluid intelligence: iRSSN obtained an $R$ value (between predicted and real values) of 0.23 ($P < 0.001$), while RSFC attained to 0.22 ($P < 0.001$), and the performance was improved to 0.31 ($P < 0.001$) when they were combined together. Figure 3E and F illustrates respective feature sets of iRSSN and RSFC that appeared in every fold of cross-validation, and the feature number ($n = 34$) of iRSSN was significantly lower than RSFC ($n = 1{,}262$). Additionally, all eight networks were involved in both iRSSN and RSFC feature sets.

## Comparison with other methods

The sMCI/pMCI classification models using atlas-based volume information achieved relatively low results (accuracy: 0.730, sensitivity: 0.605, specificity: 0.813, and AUC: 0.787), demonstrating the superiority of iRSSN than conventional morphological information in MCI subtype discrimination.

Zhao's method R2SNs is a state-of-the-art structural radiomic network, and we compared it with iRSSN comprehensively and found that (i) iRSSN (accuracy: 0.805, specificity: 0.729, specificity: 0.855, and AUC: 0.882) achieved obviously better sMCI/pMCI classification performance than R2SNs (accuracy: 0.717, sensitivity: 0.629, specificity: 0.758, and AUC: 0.786). (ii) Single R2SNs displayed similar fluid intelligence prediction performance with iRSSN, but its combination performance with RSFC was lower than iRSSN (Table 1, $P < 0.05$). Specifically, the number ($n > 4{,}000$) of features (Fig. S3) adopted by R2SNs was significantly larger than iRSSN, RSFC, and the sample size, which may indicate the potential overfitting risk. In addition, when using the same number (according to the sorted weights) of features from R2SNs as iRSSN, its prediction performance had decreased to $r = 0.16$, and the adopted features were also largely different from iRSSN.

## Other methodological considerations

Compared with the unsmoothed GM images, a 4-mm FWHM Gaussian smoothness not only improved the test–retest reliability but also enhanced the sMCI/pMCI classification: when smoothness was not adopted, a decreased mean ICC = 0.85 ($ICC_{std} = 0.03$) and a decreased sMCI/pMCI classification accuracy = 73.4% (sensitivity: 62.0%, specificity: 81.7%) were obtained. In particular, about 88.5% edges showed an ICC higher than 0.75, and about 97.6% edges showed an ICC higher than 0.60.

In addition, when comparing three different feature normalization manners, the demeaning manner achieved the best sMCI/pMCI classification performance, and the other two manners performed relatively worse (Max-Min: accuracy = 79.9%, sensitivity = 72.5%, specificity = 85.1%; Max-Min (map into [−1, 1]): accuracy = 78.9%, sensitivity = 70.5%, specificity = 84.6%) than it.

# Discussion

In this paper, we proposed a novel iRSSN from the T1 images and demonstrated it with remarkable characteristics in test–retest reliability, complex network properties and individual identification and exemplified it in two representative applications: pMCI/sMCI discrimination and fluid intelligence prediction. The results revealed that iRSSN provides a reasonable, reliable, and unique manner to understand the structural similarity in the brain, which performs better than some state-of-the-art brain networks in many aspects.

The differences between the proposed iRSSN and Zhao's method R2SNs (Zhao, Zheng, et al. 2021) are multiple: First, the preprocessing steps for T1 images between two methods are different: iRSSN adopts a series of noise reduction steps such as SANLM denoise, local intensity correction, and partial volume effect correction, while R2SNs only includes N4 bias correction before registration. Second, the registration algorithm in R2SNs is symmetric image normalization (SyN) by ANTs software, while iRSSN uses geodesic shooting registration based on CAT 12 software, which have been compared in the brain MRI registration (Ashburner and Friston 2011). Third, the used radiomic feature sets and normalization manner are also different: iRSSN adopts 43 radiomic features (including 3 intensity features and the other texture features) with a demeaning normalization, while R2SNs uses 47 radiomics features (including 13 intensity features and the other texture features) with a Max-Min normalization. The connective patterns in the structural network are thereby distinct between iRSSN and R2SNs, and Fig. 4 illustrated the connective matrix and corresponding connective value histogram for one randomly selected subject from the HCP dataset. iRSSN provides a sparser connectivity matrix than R2SNs, which is more consistent with the previous finding (Bassett and Bullmore 2006) that the brain anatomical connectivity is sparse. Specially,

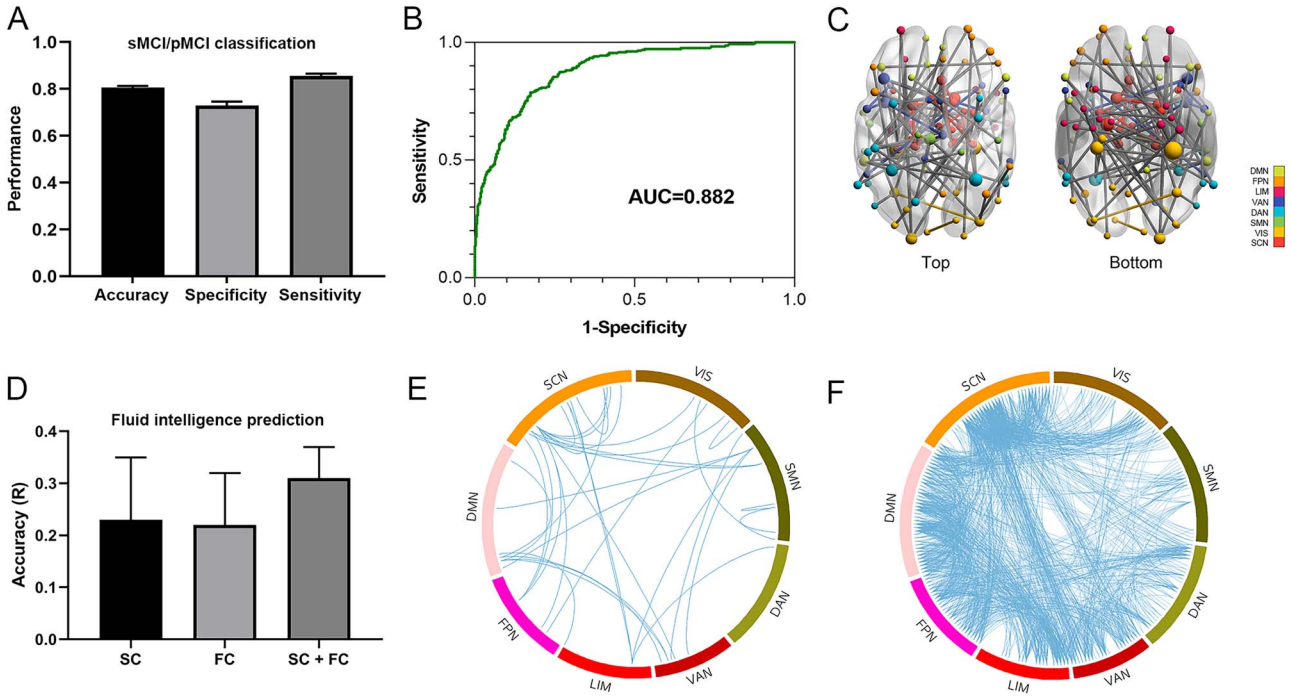


**Fig 3.** A) The classification results of sMCI and pMCI with iRSSN. B) The AUC for sMCI/pMCI discrimination. C) The discriminative features in pMCI/sMCI classification. D) The prediction accuracy of fluid intelligence. E) The discriminative features of iRSSN for fluid intelligence prediction. F) The discriminative features of RSFC for fluid intelligence prediction. Abbreviation: VIS, visual network; SMN, somatomotor network; DAN, dorsal attention network; VAN, ventral attention network; LIM, limbic network; FPN, frontoparietal network; DMN, default mode network; SCN, subcortical network.

**Table 1.** The model performance comparison in fluid intelligence prediction.

| | **iRSSN** | | **Zhao's method (R2SNs)[20]** | |
|---|---|---|---|---|
| Prediction (R value) | SC<br>0.23 ± 0.06 | SC + FC<br>**0.31 ± 0.05** | SC<br>0.23 ± 0.09 | SC + FC<br>0.27 ± 0.07 |

Abbreviation: SC, structural connectivity; FC, functional connectivity; R value: the correlation between predicted and real fluid intelligence (bold value means the highest performance).

the negative correlations exist in both iRSSN and R2SNs, which stand for the opposite radiomic feature patterns between regions. There are more negative connectivities in iRSSN that are mainly located at the subcortical nuclei, such as the thalamus, hippocampus, amygdala, and basal ganglia. Fourth, iRSSN calculates radiomics in segmented gray matter images, which can reduce the background inconsistency caused by the pathological or physiological alterations (e.g. glioma, edema) in surrounding tissues, facilitating the statistical comparisons between patients and healthy controls. With the above-mentioned differences between iRSSN and R2SNs, iRSSN displayed obvious advantages in sMCI/pMCI classification, implying the extensive applications of iRSSN in the differential diagnoses of various brain diseases. In addition, though R2SNs performs similarly with iRSSN in fluid intelligence prediction, the feature sets decided by iRSSN are extremely sparser than R2SNs, and its fusion prediction with RSFC is also better than R2SNs. These results demonstrate that iRSSN can detect more unique structural representation and better reflect the individual difference for fluid intelligence than R2SNs, resulting in more interpretable results.

iRSSN is also different from other types of structural network based on the T1 image. Tijms' method (Tijms et al. 2012) quantifies the relationship between predefined cubes from T1 image; however, the position of these cubes doesn't comply with the anatomical border of brain regions, which may limit the interpretation of network nodes in the network. Another common type of structural network uses multiple morphological features (Li, Yang, et al. 2017; Seidlitz et al. 2018) as a vector for network construction. These morphological features are usually calculated on the vertex-based surface space, which is more time-consuming than the voxel-based volume space. In addition, these features belong to macroscopic descriptors in contrast to texture features, thus ignoring the microscopic viewpoint within the image. Taken together, iRSSN is an anatomically interpretable individualized structural network that incorporates both microstructural and macrostructural characteristics.

Although the definite physiological significance of iRSSN is unclear, it has been reported that radiomic features record the subtle alterations within the image, which are related with the synaptic, genetic, and cellular characteristics (Alexander-Bloch et al. 2013). Moreover, iRSSN has typical characteristics of a good imaging biomarker: high test–retest reliability and fingerprinting performance, which are very essential for individualized clinical diagnosis. Moreover, iRSSN displays similar complex network properties as other well-known brain biological networks (Achard and Bullmore 2007; Gong et al. 2009; Cai et al. 2018), such as the small-worldness, indicating that it is like a biologically meaningful and economical brain network. With the increase of sparsity thresholds, the characteristic path length of iRSSN becomes smaller, while the clustering coefficient and local and

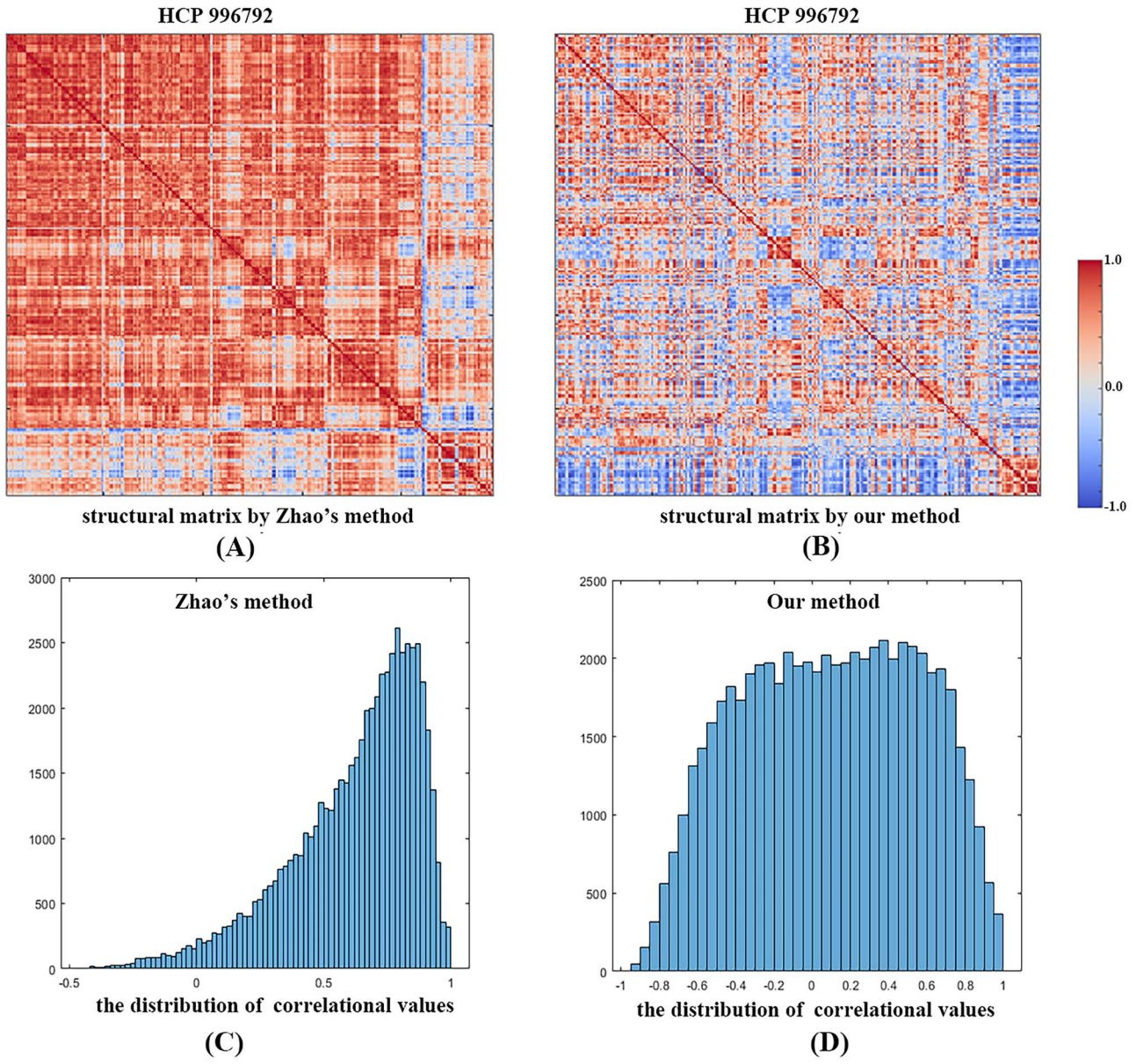


**Fig. 4.** The connectivity matrix and the corresponding histogram of correlational values of the structural network generated by our method (iRSSN) and Zhao's method (R2SNs) on a randomly selected HCP subject (ID: 996792) A) structural matrix by R2SNs. B) Structural matrix by iRSSN. C) The histogram of correlational values in Fig. 4A. D) The histogram of correlational values in Fig. 4B.

global efficiency become larger. These changing patterns coincide with other brain networks like RSFC, demonstrating that iRSSN is a reasonable structural brain network. In addition, the degree distribution of iRSSN shows an exponentially truncated power-law form, implying the existence of hub regions and module in iRSSN. The hub regions are mainly located at the precuneus, thalamus, basal ganglia, superior temporal gyrus, cingulate gyrus, and middle temporal gyrus, which are partly consistent with hubs (Bell and Shine 2016; Oldham and Fornito 2019) in other networks of the adult brain. These hub regions are involved in lots of cognitive and behavioral domains, such as self-awareness (Lou et al. 2017), cognitive computation (Rikhye et al. 2018), speech processing (Yi et al. 2019), language (Nadeau 2021), and prosocial behavior (Lockwood et al. 2020). Furthermore, the spatial distribution of iRSSN modules is largely different from the RSFC modules, and the largest spatial overlap between any module in iRSSN and RSFC is just with a dice coefficient of 0.46, again indicating that iRSSN may provide a unique perspective to understand the brain in contrast to RSFC, which could be extended to various individualized prediction tasks with the fusion manner.

To timely recognize pMCI from sMCI patients is clinically important but challenging, and most studies have achieved the classification accuracies lower than 0.80 (Lian et al. 2020; Zhou et al. 2020). For comparison, we also used the atlas-based volume information for sMCI/pMCI classification, and the model just obtained an accuracy of 0.730; thus, only the conventional morphological information is not enough for effective sMCI/pMCI classification. A possible reason may be due to the adopted macroscopic structural features (e.g. volume, cortical thickness), which may thus lose some sensitive microscopic angle for diagnosis. In contrast, iRSSN obtained an inspiring accuracy of 0.805 and an AUC of 0.882, and a total of 91 discriminative features were found. Many of the connective features were internetwork and long range, involving the dorsal/ventral attention network, default mode network, and visual network, and the related key

hubs were the bilateral parahippocampus, right hippocampus, and left superior parietal lobule. These findings were persistently reported in MCI patients (Liu et al. 2016; Li, Jing, et al. 2017; Long et al. 2018; Ma et al. 2020), and future studies can further combine iRSSN with other brain networks together to improve the diagnostic accuracy for pMCI patients.

It should be mentioned that several factors may affect iRSSN and its clinical applications. First, smoothness is found to be helpful for iRSSN in improving both test–retest reliability and the sMCI/pMCI classification. One possible explanation is that smoothness can effectively suppress image noise, leading to more accordant radiomic features among subjects. Second, the feature normalization manner for iRSSN also influenced the sMCI/pMCI classification, and the demeaning manner achieved the best performance. However, we infer that the optimal feature normalization manner may be task specific. Once iRSSN is utilized for another task or dataset, the normalization manner should be optimized again. Third, the ideal radiomic feature sets to construct iRSSN is not assessed, and further studies can be carried out to ascertain whether better performance would be achieved when using other features.

Some limitations exist in the current study. First, for clinical T1 images, the strength of the MRI scanner and the initial/normalized voxel size of the T1 image are commonly not identical at different centers/hospitals, and it is unknown whether these factors may affect iRSSN. Second, the multicenter test–retest dataset in the study adopted a more time-consuming MP2RAGE sequence compared with the conventional MPRAGE sequence, which may be another influencing factor. Third, iRSSN is just limited in the gray matter of the brain; however, white matter has also been reported to have an important role in brain function (Wang et al. 2022). Therefore, iRSSN can extend to white matter to explore their usages in phenotype prediction and clinical diagnosis in future. Fourth, the study just compares iRSSN with RSFC in some ways, but the correlations with other types of brain networks like the brain fiber network from diffusion tensor imaging and the metabolic network from positron emission tomography are still unknown, which need further studies afterward.

## Conclusion

In this paper, we introduced a novel individualized radiomics-based structural connectivity metric called iRSSN, and it displayed good complex network properties and biomarker attributes and achieved inspiring performances in sMCI/pMCI discrimination and fluid intelligence prediction. Overall, our study suggested that iRSSN could uncover distinct brain structural relationships complementary to the widely used RSFC, which has significant potential in various phenotypic predictions and disease classifications.

## Acknowledgments

Private sector contributions are facilitated by the Foundation for the National Institutes of Health (www.fnih.org). The grantee organization is the Northern California Institute for Research and Education, and the study is coordinated by the Alzheimer's Therapeutic Research Institute at the University of Southern California. ADNI data are disseminated by the Laboratory for Neuro Imaging at the University of Southern California.

## CRediT author statement

Han Liu (Formal analysis, Investigation, Methodology, Resources, Writing—original draft), Zhe Ma (Formal analysis, Investigation, Methodology), Lijiang Wei (Formal analysis, Investigation), Zhenpeng Chen (Formal analysis, Methodology), Yun Peng (Funding acquisition, Project administration, Supervision, Writing—review & editing), Zhicheng Jiao (Conceptualization, Methodology, Writing—review & editing), Harrison X. (Bai Conceptualization, Investigation, Writing—review & editing), and Bin Jing (Conceptualization, Formal analysis, Investigation, Supervision, Writing—original draft, Writing—review & editing)

## Supplementary material

Supplementary material is available at *Cerebral Cortex* online.

## Funding

This work was supported by Beijing Hospitals Authority's Ascent Plan, Code: DFL20221002, National Natural Science Foundation of China 12171330, STI 2030—Major Projects 2021ZD0200508, Beijing Municipal Commission of Education, Grant/Award Number: KM202010025025, and Open fund project of Beijing Key Laboratory of Fundamental Research on Biomechanics in Clinical Application (2023KF05). Data collection and sharing for this project were funded by the Alzheimer's Disease Neuroimaging Initiative (ADNI) (National Institutes of Health Grant U01 AG024904) and DOD ADNI (Department of Defense award number W81XWH-12-2-0012). ADNI is funded by the National Institute on Aging, the National Institute of Biomedical Imaging and Bioengineering, and through generous contributions from the following: AbbVie, Alzheimer's Association; Alzheimer's Drug Discovery Foundation; Araclon Biotech; BioClinica, Inc.; Biogen; Bristol-Myers Squibb Company; CereSpir, Inc.; Cogstate; Eisai Inc.; Elan Pharmaceuticals, Inc.; Eli Lilly and Company; EuroImmun; F. Hoffmann-La Roche Ltd and its affiliated company Genentech, Inc.; Fujirebio; GE Healthcare; IXICO Ltd; Janssen Alzheimer Immunotherapy Research & Development, LLC.; Johnson & Johnson Pharmaceutical Research & Development LLC.; Lumosity; Lundbeck; Merck & Co., Inc.; MesoScale Diagnostics, LLC.; NeuroRx Research; Neurotrack Technologies; Novartis Pharmaceuticals Corporation; Pfizer Inc.; Piramal Imaging; Servier; Takeda Pharmaceutical Company; and Transition Therapeutics. The Canadian Institutes of Health Research is providing funds to support ADNI clinical sites in Canada.

*Conflict of interest statement*: None declared.

## Data availability

The datasets used and analyzed in the current study are available from open-source Human Connectome Project (https://www.humanconnectome.org/), Alzheimer's disease Neuroimaging Initiative repository (http://www.loni.ucla.edu/ADNI), and Multicenter dataset of healthy traveling adults with identical settings (https://doi.org/10.6084/m9.figshare.8851955).

## References

Achard S, Bullmore ET. Efficiency and cost of economical brain functional networks. *PLoS Comput Biol*. 2007:3(2):174–183.

Alexander-Bloch A, Giedd JN, Bullmore E. Imaging structural co-variance between human brain regions. *Nat Rev Neurosci*. 2013:14(5):322–336.

Ashburner J. A fast diffeomorphic image registration algorithm. *NeuroImage*. 2007:38(1):95–113.

Ashburner J, Friston KJ. Unified segmentation. *NeuroImage*. 2005:26(3):839–851.

Ashburner J, Friston KJ. Diffeomorphic registration using geodesic shooting and gauss-Newton optimisation. *NeuroImage*. 2011:55(3): 954–967.

Bassett DS, Bullmore E. Small-world brain networks. *Neuroscientist*. 2006:12:512–523.

Bell PT, Shine JM. Subcortical contributions to large-scale network communication. *Neurosci Biobehav Rev*. 2016:71:313–322.

Buimer EEL, Pas P, Brouwer RM, Froeling M, Hoogduin H, Leemans A, Luijten P, van Nierop BJ, Raemaekers M, Schnack HG, et al. The YOUth cohort study: MRI protocol and test-retest reliability in adults. *Dev Cogn Neurosci*. 2020:45:100816.

Bullmore ET, Sporns O. Complex brain networks: graph theoretical analysis of structural and functional systems. *Nat Rev Neurosci*. 2009:10:186–198.

Cai L, Dong Q, Niu HJ. The development of functional network organization in early childhood and early adolescence: a resting-state fNIRS study. *Dev Cogn Neurosci*. 2018:30:223–235.

Chen PY, Chen CL, Hsu YC, Cam CAN, Tseng WI. Fluid intelligence is associated with cortical volume and white matter tract integrity within multiple-demand system across adult lifespan. *NeuroImage*. 2020:212:116576.

Fan L, Li H, Zhuo J, Zhang Y, Wang J, Chen L, Yang Z, Chu C, Xie S, Laird AR, et al. The human Brainnetome atlas: a new brain atlas based on connectional architecture. *Cereb Cortex*. 2016:26:3508–3526.

Feng P, Jiang R, Wei L, Calhoun VD, Jing B, Li H, Sui J. Determining four confounding factors in individual cognitive traits prediction with functional connectivity: an exploratory study. *Cereb Cortex*. 2022:33(5):2011–2020.

Finn ES, Shen X, Scheinost D, Rosenberg MD, Huang J, Chun MM, Papademetris X, Constable RT. Functional connectome fingerprinting: identifying individuals using patterns of brain connectivity. *Nat Neurosci*. 2015:18:1664–1671.

Gong GL, He Y, Concha L, Lebel C, Gross DW, Evans AC, Beaulieu C. Mapping anatomical connectivity patterns of human cerebral cortex using in vivo diffusion tensor imaging Tractography. *Cereb Cortex*. 2009:19(3):524–536.

Jiang T. Brainnetome: a new -ome to understand the brain and its disorders. *NeuroImage*. 2013:80:263–272.

Jiang R, Calhoun VD, Cui Y, Qi S, Zhuo C, Li J, Jung R, Yang J, Du Y, Jiang T, et al. Multimodal data revealed different neurobiological correlates of intelligence between males and females. *Brain Imaging Behav*. 2020:14(5):1979–1993.

Jiang R, Calhoun VD, Fan L, Zuo N, Jung R, Qi S, Lin D, Li J, Zhuo C, Song M, et al. Gender differences in connectome-based predictions of individualized intelligence quotient and sub-domain scores. *Cereb Cortex*. 2020:30(3):888–900.

Jing B, Liu B, Li H, Lei J, Wang Z, Yang Y, Sun PZ, Xue B, Liu H, Xu ZD. Within-subject test-retest reliability of the atlas-based cortical volume measurement in the rat brain: a voxel-based morphometry study. *J Neurosci Methods*. 2018:307:46–52.

Kong XZ, Wang X, Huang L, Pu Y, Yang Z, Dang X, Zhen Z, Liu J. Measuring individual morphological relationship of cortical regions. *J Neurosci Methods*. 2014:237:103–107.

Kong XZ, Liu Z, Huang L, Wang X, Yang Z, Zhou G, Zhen Z, Liu J. Mapping individual brain networks using statistical similarity in regional morphology from MRI. *PLoS One*. 2015:10(11): e 0141840.

Kuo CY, Lee PL, Hung SC, Liu LK, Lee WJ, Chung CP, Yang AC, Tsai SJ, Wang PN, Chen LK, et al. Large-scale structural covariance networks predict age in middle-to-late adulthood: a novel brain aging biomarker. *Cereb Cortex*. 2020:30(11):5844–5862.

Lambin P, Leijenaar RTH, Deist TM, Peerlings J, de Jong EEC, van Timmeren J, Sanduleanu S, Larue R, Even AJG, Jochems A, et al. Radiomics: the bridge between medical imaging and personalized medicine. *Nat Rev Clin Oncol*. 2017:14(12):749–762.

Latora V, Marchiori M. Efficient behavior of small-world networks. *Phys Rev Lett*. 2001:87(19):198701.

Li W, Yang C, Shi F, Wu S, Wang Q, Nie Y, Zhang X. Construction of individual morphological brain networks with multiple morphometric features. *Front Neuroanat*. 2017:11:34.

Li YX, Jing B, Liu H, Li YF, Gao X, Li YQ, Mu B, Yu HK, Cheng J, Barker PB, et al. Frequency-dependent changes in the amplitude of low-frequency fluctuations in mild cognitive impairment with mild depression. *J Alzheimers Dis*. 2017:58(4):1175–1187.

Li Y, Wang N, Wang H, Lv Y, Zou Q, Wang J. Surface-based single-subject morphological brain networks: effects of morphological index, brain parcellation and similarity measure, sample size-varying stability and test-retest reliability. *NeuroImage*. 2021:235:118018.

Lian C, Liu M, Zhang J, Shen D. Hierarchical fully convolutional network for joint atrophy localization and Alzheimer's disease diagnosis using structural MRI. *IEEE Trans Pattern Anal Mach Intell*. 2020:42(4):880–893.

Liu MX, Zhang DQ, Shen DG. Relationship induced multi-template learning for diagnosis of Alzheimer's disease and mild cognitive impairment. *IEEE Trans Med Imaging*. 2016:35(6):1463–1474.

Liu J, Wang J, Tang Z, Hu B, Wu FX, Pan Y. Improving Alzheimer's disease classification by combining multiple measures. *IEEE/ACM Trans Comput Biol Bioinform*. 2018:15(5):1649–1659.

Liu H, Jing B, Han W, Long Z, Mo X, Li H. A comparative texture analysis based on NECT and CECT images to differentiate lung adenocarcinoma from squamous cell carcinoma. *J Med Syst*. 2019:43(3):59.

Liu Z, Wang S, Dong D, Wei J, Fang C, Zhou X, Sun K, Li L, Li B, Wang M, et al. The applications of Radiomics in precision diagnosis and treatment of oncology: opportunities and challenges. *Theranostics*. 2019:9(5):1303–1322.

Liu H, Jiao Z, Han W, Jing B. Identifying the histologic subtypes of non-small cell lung cancer with computed tomography imaging: a comparative study of capsule net, convolutional neural network, and radiomics. *Quant Imaging Med Surg*. 2021:11(6): 2756–2765.

Lockwood PL, O'Nell KC, Apps MAJ. Anterior cingulate cortex: a brain system necessary for learning to reward others? *PLoS Biol*. 2020:18(6):18.

Long ZQ, Huang JC, Li B, Li ZJ, Li ZH, Chen HW, Jing B. A comparative atlas-based recognition of mild cognitive impairment with voxel-based morphometry. *Front Neurosci*. 2018:12:916.

Lou HC, Changeux JP, Rosenstand A. Towards a cognitive neuroscience of self-awareness. *Neurosci Biobehav Rev*. 2017:83:765–773.

Ma Z, Jing B, Li YX, Yan HG, Li ZX, Ma XY, Zhuo ZZ, Wei LJ, Li HY, AsD N. Identifying mild cognitive impairment with random forest by integrating multiple MRI morphological metrics. *J Alzheimers Dis*. 2020:73(3):991–1002.

Manjon JV, Coupe P, Marti-Bonmati L, Collins DL, Robles M. Adaptive non-local means denoising of MR images with spatially varying noise levels. *J Magn Reson Imaging*. 2010:31(1):192–203.

Nadeau SE. Basal ganglia and thalamic contributions to language function: insights from a parallel distributed processing perspective. *Neuropsychol Rev*. 2021:31(3):495–515.

Newman ME. Modularity and community structure in networks. *Proc Natl Acad Sci U S A*. 2006:103(23):8577–8582.

Oldham S, Fornito A. The development of brain network hubs. *Dev Cogn Neurosci*. 2019:36:100607.

Rikhye RV, Wimmer RD, Halassa MM. Toward an integrative theory of thalamic function. *Annu Rev Neurosci*. 2018:41(41):163–183.

Seidlitz J, Vasa F, Shinn M, Romero-Garcia R, Whitaker KJ, Vertes PE, Wagstyl K, Kirkpatrick Reardon P, Clasen L, Liu S, et al. Morphometric similarity networks detect microscale cortical organization and predict inter-individual cognitive variation. *Neuron*. 2018:97:231–247.e7.

Tijms BM, Series P, Willshaw DJ, Lawrie SM. Similarity-based extraction of individual networks from gray matter MRI scans. *Cereb Cortex*. 2012:22(7):1530–1541.

Tohka J, Zijdenbos A, Evans A. Fast and robust parameter estimation for statistical partial volume models in brain MRI. *NeuroImage*. 2004:23(1):84–97.

Tomaszewski MR, Gillies RJ. The biological meaning of Radiomic features. *Radiology*. 2021:298(3):505–516.

Tong Q, He H, Gong T, Li C, Liang P, Qian T, Sun Y, Ding Q, Li K, Zhong J. Multicenter dataset of multi-shell diffusion MRI in healthy traveling adults with identical settings. *Sci Data*. 2020:7(1):157.

Vallieres M, Freeman CR, Skamene SR, El Naqa I. A radiomics model from joint FDG-PET and MRI texture features for the prediction of lung metastases in soft-tissue sarcomas of the extremities. *Phys Med Biol*. 2015:60(14):5471–5496.

Wang J, Wang L, Zang Y, Yang H, Tang H, Gong Q, Chen Z, Zhu C, He Y. Parcellation-dependent small-world brain functional networks: a resting-state fMRI study. *Hum Brain Mapp*. 2009:30(5):1511–1523.

Wang H, Jin X, Zhang Y, Wang J. Single-subject morphological brain networks: connectivity mapping, topological characterization and test-retest reliability. *Brain Behav*. 2016:6(4):e00448.

Wang XH, Jiao Y, Li L. A unified framework for mapping individual interregional high-order morphological connectivity based on regional cortical features from anatomical MRI. *Magn Reson Imaging*. 2020:66:232–239.

Wang P, Wang JL, Michael A, Wang ZD, Klugah-Brown B, Meng C, Biswal BB. White matter functional connectivity in resting-state fMRI: robustness, reliability, and relationships to gray matter. *Cereb Cortex*. 2022:32(8):1547–1559.

Watts DJ, Strogatz SH. Collective dynamics of 'small-world' networks. *Nature*. 1998:393(6684):440–442.

Wei L, Jing B, Li H. Bootstrapping promotes the RSFC-behavior associations: an application of individual cognitive traits prediction. *Hum Brain Mapp*. 2020:41(9):2302–2316.

Wu W, Parmar C, Grossmann P, Quackenbush J, Lambin P, Bussink J, Mak R, Aerts HJ. Exploratory study to identify radiomics classifiers for lung cancer histology. *Front Oncol*. 2016:6:71.

Yeo BT, Krienen FM, Sepulcre J, Sabuncu MR, Lashkari D, Hollinshead M, Roffman JL, Smoller JW, Zollei L, Polimeni JR, et al. The organization of the human cerebral cortex estimated by intrinsic functional connectivity. *J Neurophysiol*. 2011:106(3):1125–1165.

Yi HG, Leonard MK, Chang EF. The encoding of speech sounds in the superior temporal gyrus. *Neuron*. 2019:102(6):1096–1110.

Yu K, Wang X, Li Q, Zhang X, Li X, Li S. Individual morphological brain network construction based on multivariate Euclidean distances between brain regions. *Front Hum Neurosci*. 2018:12:204.

Yun JY, PSW B, Vriend C, Jahanshad N, Abe Y, Ameis SH, Anticevic A, Arnold PD, Batistuzzo MC, Benedetti F, et al. Brain structural covariance networks in obsessive-compulsive disorder: a graph analysis from the ENIGMA consortium. *Brain*. 2020:143:684–700.

Zhao J, Ma Z, Chen F, Li L, Ren M, Li A, Jing B, Li H. Human immune deficiency virus-related structural alterations in the brain are dependent on age. *Hum Brain Mapp*. 2021:42(10):3131–3140.

Zhao K, Zheng Q, Che T, Martin D, Li Q, Ding Y, Zheng Y, Liu Y, Li S. Regional radiomics similarity networks (R2SNs) in the human brain: reproducibility, small-world properties and a biological basis. *Netw Neurosci*. 2021:5(3):783–797.

Zhou T, Thung KH, Liu M, Shi F, Zhang C, Shen D. Multi-modal latent space inducing ensemble SVM classifier for early dementia diagnosis with neuroimaging data. *Med Image Anal*. 2020:60:101630.